Computers and Concrete, Vol. 8, No. 4 (2011) 401-423
DOI: http://dx.doi.org/10.12989/cac.2011.8.4.401

A mesoscale model for concrete to simulate mechanical failure

Jörg F. Unger*, Stefan Eckardt and Carsten Könke

Institute of Structural Mechanics, Bauhaus University Weimar, Marienstr. 15, D-99423 Weimar, Germany

(Received February 16, 2009, Accepted August 16, 2010)

Abstract. In this paper, a mesoscale model of concrete is presented, which considers particles, matrix material and the interfacial transition zone (ITZ) as separate constituents. Particles are represented as ellipsoides, generated according to a prescribed grading curve and placed randomly into the specimen. In this context, an efficient separation procedure is used. The nonlinear behavior is simulated with a cohesive interface model for the ITZ and a combined damage/plasticity model for the matrix material. The mesoscale model is used to simulate a compression and a tensile test. Furthermore, the influence of the particle distribution on the loaddisplacement curve is investigated.

Keywords: mesoscale; concrete.

1. Introduction

A simulation of concrete on the macroscale allows a characterization of the homogenized response on lower scales, but the true physical phenomena can only be represented in a phenomenological approach. This often requires complex material formulations with many parameters, which are often difficult to be determined. The modeling of concrete on the mesoscale allows for the direct representation of the heterogenous structure (Häfner *et al.* 2006), including e.g. the mass fraction and the grading curve of particles, the shape of the particles (Carpinteri and Chiaia 1995), the interfacial transition zone (ITZ) at the interface between particles and matrix material and a separate constitutive formulation for each of the individual constituents (particles, mortar matrix, ITZ).

For numerical simulations, two approaches to describe the mesostructure can be distinguished. On the one hand, real specimens can be analyzed and, by using digital image analysis, equivalent numerical models can be built (Nagai *et al*. 2000). On the other hand, a functional description of the grading curve and the particle shape allows the generation of random samples of the heterogenous microstructure (Wang *et al*. 1999), which allows the investigation of statistical effects.

The first mesoscale models of concrete are based on the lattice approach (Schlangen 1993, Vervuurt 1997, Chiaia *et al*. 1997, Leite *et al*. 2004). According to the position in the model, a material (particle, matrix, ITZ) is assigend to each lattice. The properties of the beam elements, which might include a stochastic component, are derived from macroscopic properties such as Young's modulus or Poisson's ratio. Different approaches to model the failure of a single lattice have been investigated. One possibility is the so called tension cut-off, where the lattice is removed from the

* Corresponding author, Ph.D., E-mail: joerg.unger@uni-weimar.de

model, if the prescribed tensile strength is exceeded. However, this leads to spurious steps in the load-displacement curve each time a lattice is removed. In another approach, a linear model for the prepeak region combined with a softening function is used (Grassl and Bažant 2009). The primary problem of these approaches is the determination of the material parameters, since no direct relation between the properties of the lattice and the obtained macroscopic properties can be derived.

A second group are particle methods, which can be used for the simulation of cohesive granular materials (d'Addetta 2002). Particles are simulated as discontinous spheres, where the interaction between neighboring particles is solely determined by their relative spatial position. A similar difficult problem is here the determination of material parameters for the description of the cohesion between the particles.

A third group are continuum models (Wriggers and Moftah 2006, Eckardt and Könke 2006), where the mesostructure is explicitly represented. In this context, it is assumed that simple material models can be used, since the complexity of the response is additionally included in the complex heterogenous geometric description of the material. Furthermore, the nonlinear behavior of the ITZ at the interface between mortar matrix and particle can directly be simulated, e.g. with a cohesive model. Generally, a discretization with an aligned mesh is used for this purpose. In (Sukumar *et al.* 2001, Unger and Könke 2006), a procedure using the XFEM approach in combination with levelsets is used to model the ITZ, which allows the application of a regular quadrilateral mesh. In (Carol *et al.* 2002) it is assumed that the nonlinear behavior can solely be described by a nonlinear model for the interface. For that purpose, a mesoscale model with linear elastic particles is meshed with triangular elements, and interface elements are placed between each finite element. The disadvantage of this approach is that the crack path is limited to the element edges and a strong mesh dependency is obtained.

Advantageous of all mesoscale models is the fact that the complex macroscopic material behavior can be described by simple material formulations of each constituent on the mesoscale. An example is the nonlinear prepeak region in a tensile test, which can be described on the mesoscale without any hardening variables. Furthermore, the artificial insertion of a weak point to initiate localization as e.g. in a uniaxial tensile test can be avoided, since, due to the heterogenous structure on the mesoscale, stress concentrations and, consequently, zones of local damage naturally occur.

2. Modeling of the geometry

An important aspect of the mesoscale simulation of concrete is the exact representation of the particle shapes, their size distribution according to a prescribed grading curve and the spatial position and orientation of the particles within the specimen. Two main concepts to build a numerical mesoscale model of concrete can be distinguished. The first possibility is based on image processing techniques. Based on a X-ray computer tomography (Feldkamp *et al.* 1989) or by sequential sectioning and 2-D image processing (Takano *et al.* 2003) a 3-dimensional voxel representation of the microstructure is obtained, which can be used in a voxel based finite element representation (Hollister and Kikuchi 1994, Nagai *et al.* 2000, Nagano *et al.* 2004). A second approach, followed in this thesis, is the artificial generation of the microstructure. (Zaitsev and Wittmann 1981) used polygonal and spherical inclusions to simulate concrete on the mesoscale. For 3-dimensional models, either spheres (Bazant *et al.* 1990, Schlangen and van Mier 1992) or ellipsoides (Häfner *et al.* 2003, Leite *et al.* 2004, 2007) are common shapes to describe the aggregates. (Garboci 2002) used voxel representations of

real concretes to describe the size and shape of aggregates in concrete by spherical harmonics, which allows the simulation of random shapes.

In order to obtain realistic models, certain statistical characteristics of the real model, e.g. the size distribution of particles has to be represented in the numerical model. The size distribution of particles is commonly characterized by a grading curve. Grading curves for standardized concrete are defined in the design codes. A grading curve is defined by aperture sizes of a set of sieves and the corresponding mass fraction that passes through these sieves. An alternative approach is the description of the size distribution using an explicit function such as e.g. Fuller's curve. Using many different sieves, the second approach (Fuller) can almost exactly be reproduced by the first approach.

In the current implementation, an algorithm similar to (Eckardt and Könke 2008) is used. It can be divided into the generation of the correct set of particles and, afterwards, the placing of these particles into the specimen, which is commonly refered to as the set and place method.

2.1 Sampling of particles according to a size distribution

Particles are simplified by ellipsoids and the generation of the geometry is fully performed in 3-D. A 2-dimensional model can be obtained by cutting a slice out of the 3-dimensional model. In the local coordinate system aligned with the principal axis, the surface of an ellipsoid is defined by

$$\sum_{i=1}^{3}\left(\frac{x_i}{r_i}\right)^2 = 1 \tag{1}$$

where r_i are the principal radii. Without loss of generality, it is assumed that $r_1 \geq r_2 \geq r_3$. It is further assumed that a particle passes through a sieve, if its medium diameter $2r_2$ is smaller than the aperture of the sieve.

The radii r_1 and r_3 are determined from r_2 according to

$$r_1 = \left(1 + u_1 \frac{m-1}{m+1}\right) r_2 \tag{2}$$

$$r_3 = \left(1 - u_3 \frac{m-1}{m+1}\right) r_2 \tag{3}$$

where u_1 and u_2 are realizations of random variables U_1, U_3 which are uniformly distributed in the interval [0, 1] and m is a constant that characterizes the flatness of the ellipsoids. For $m = 1$, all radii are identical and the ellipsoids reduce to spheres, whereas for higher values the flatness increases. The assumptions of a linear distribution of r_1 and r_3 in the intervals $\left[r_2, r_2 \frac{2m}{m+1}\right]$ and $\left[r_2 \frac{2}{m+1}, r_2\right]$ has been made for simplicity, but any other distribution can be used. The expected volume $E(V)$ of a particle is then given by

$$E(V) = \int_{u_1=-\infty}^{\infty} \int_{u_3=-\infty}^{\infty} \frac{4}{3}\pi^3 r_1(u_1, r_2) r_2 r_3(u_3, r_2) du_3 du_1 \tag{4}$$

Since the variables U_1 and U_3 are independent and uniformly distributed in the interval [0,1], Eq. (4) can be simplified to

$$E(V) = \int_{u_1=0}^{1} \int_{u_3=0}^{1} \frac{4}{3}\pi^3 r_2^3 \left(1+u_1\frac{m-1}{m+1}\right)\left(1-u_3\frac{m-1}{m+1}\right) du_3 du_1 \tag{5}$$

$$= \frac{4}{3}\pi^3 r_2^3 \left[1-\left(\frac{m-1}{2(m+1)}\right)^2\right] \tag{6}$$

In the grading curve, different mineralsize classes i can be dinstinguished, each having a minimum diameter d^i_{min} and a maximum diameter d^i_{max}. From the total mass of particles m_{tot} and the grading curve, the mass of each mineralsize class can be determined

$$m_i = m_{tot}[F_m(d^i_{max}) - F_m(d^i_{min})] \tag{7}$$

where $F_m(d)$ is the ratio of mass passing through a sieve of aperture size d and the total mass. Consequenstly, each class can be simulated separately and the index i is omitted. The function $F_m(d)$ can be interpreted as the cumulated probability density function of the mass distribution as a function of the diameter $d_2 = 2r_2$. Assuming a linear function in the logarithmic scale between $F_m(d_{min}) = 0$ and $F_m(d_{max}) = 1$, it follows

$$F_m(d_2) = \frac{\ln(d_2) - \ln(d_{min})}{\ln(d_{max}) - \ln(d_{min})} \quad \text{with} \quad d_{min} \le d_2 \le d_{max} \tag{8}$$

This can be interpreted as the accumulated probability density function of the mass as a function of the diameter d_2. The corresponding probability density function is obtained by differentiation of Eq. (8)

$$\phi_m(d_2) = \frac{\partial F_m(d_2)}{\partial d_2} = \frac{1}{d_2[\ln(d_{max}) - \ln(d_{min})]} \tag{9}$$

Eq. (9) describes the mass distribution within the mineral size class. From the mass distribution, the distribution for the number of particles is derived. The mass of particles M of size d_2 is given by

$$M(d_2) = n(d_2)\rho E(V(d_2)) \tag{10}$$

where $n(d_2)$ is the number of particles with diameter d_2, ρ is the density of the particles assumed to be identical for all mineral size classes and $E(V(d_2))$ is the expected value of the volume of a particle with diameter d_2 given in Eq. (6) with $2r_2 = d_2$. Consequently, the distribution of the number of particles as a function of the radius d_2 is given by

$$\phi_n(d_2) = \frac{\dfrac{\phi_m(d_2)}{\rho E(V(d_2))}}{\displaystyle\int_{x=d_{min}}^{d_{max}} \frac{\phi_m(x)}{\rho E(V(x))}\, dx} \tag{11}$$

where the denominator corresponds to the total number of particles in the interval $[d_{min}, d_{max}]$. Substitution of Eq. (6) and simplification finally gives

$$\phi_n(d_2) = \frac{3 d^3_{max} d^3_{min}}{d_2^4 (d^3_{max} - d^3_{min})} \tag{12}$$

which describes the density function for the number of ellipsoides. Integration of the density function gives the cumulated density function of the ellipsoides

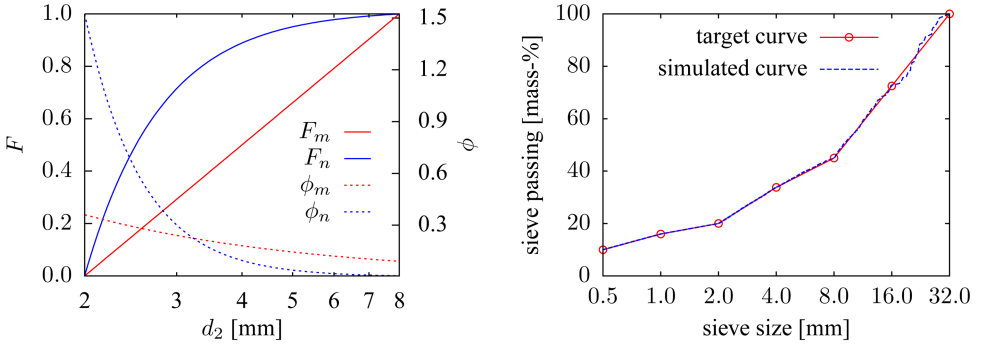

(a) Cdf F and pdf ϕ of the distributions for mass m and number of samples n in the mineral size class 2-8

(b) Comparison of target and simulated grading curves

Fig. 1 Sampling of particles according to a prescribed grading curve

$$F_n(d_2) = \int_{x=d_{min}}^{d_2} \phi_n(x) = \frac{d_{max}^3 d_{min}^3}{d_{max}^3 - d_{min}^3}\left(\frac{1}{d_{min}^3} - \frac{1}{d_2^3}\right) \tag{13}$$

In order to simulate particles according to the prescribed cumulative distribution function, the inversion method is used, which means sampling a uniform random variable U_2 in the range [0, 1] and then using the inverse function of the cumulated distribution function to obtain the corresponding diameter d_2

$$d_2 = \frac{d_{max} d_{min}}{\sqrt[3]{u_2 d_{min}^2 + (1-u_2) d_{max}^3}} \tag{14}$$

The procedure is illustrated for the mineral size class [2, 8] in Fig. 1. Note that F_m is a linear function in the logarithmic scale, whereas F_n is nonlinear. In a similar way, it is observed that the density function ϕ_m is much smaller than ϕ_n for small diameters d_2. This is due to the fact that, for a smaller diameter d_2, in order to have the same mass proportion a much higher number of samples is required.

The take process can be summarized as follows. Starting with the largest mineralsize class, particles are generated by sampling random numbers u_1, u_2 and u_3 in the interval [0, 1]. From these samples, the principal diameters/radii of the particle using Eqs. (14), (2) and (3) are calculated. The procedure is repeated until the mass m_i is exceeded. The difference between the simulated mass $\overline{m}_i$ and the target mass m_i is subtracted from the next mineral size class in order to ensure that the total simulated mass is almost identical to its target value.

2.2 Placing the particles

After having created the particles for a prescribed volume, the particles are placed into the specimen at a random position and with random orientation, which are assumed to be uniformly distributed in their domain. For a 3-dimension simulation, this corresponds to three coordinates and three orientation angles. In order to avoid overlapping between particles and the boundary of the domain and overlapping between neighboring particles, separation checks have to be performed.

From the computational point of view, the most expensive procedure is the separation between particles, which is due to the large number of particles considered. At first, the bounding boxes of the ellipsoides are checked and in the case of their intersection, an efficient separation check for ellipsoides developed by (Wang *et al.* 2001) is applied. The representation of two ellipsoids $\mathcal{A}$ and $\mathcal{B}$ from Eq. (1) is rewritten as

$$\mathcal{A}: 0 = \boldsymbol{x}^T \boldsymbol{A} \boldsymbol{x} \tag{15}$$

$$\mathcal{B}: 0 = \boldsymbol{x}^T \boldsymbol{T}^T \boldsymbol{B} \boldsymbol{T} \boldsymbol{x} \tag{16}$$

with $\boldsymbol{x} = (x_1, x_2, x_3, 1)$ being homogenous coordinates,

$$A = \mathrm{diag}(1/(r_1^{\mathcal{A}})^2, 1/(r_2^{\mathcal{A}})^2, 1/(r_3^{\mathcal{A}})^2, -1) \tag{17}$$

$$B = \mathrm{diag}(1/(r_1^{\mathcal{B}})^2, 1/(r_2^{\mathcal{B}})^2, 1/(r_3^{\mathcal{B}})^2, -1) \tag{18}$$

and $\boldsymbol{T}$ a transformation matrix that maps the ellipsoid $\mathcal{B}$ into the coordinate system aligned with the principal axes of $\mathcal{A}$. The characteristic polynomial is defined as

$$f(\lambda) = \det(\lambda \mathbf{A} + \mathbf{B}) \tag{19}$$

and $f(\lambda)$ is called the characteristic equation. (Wang *et al.* 2001) showed that two ellipsoids $\mathcal{A}$ and $\mathcal{B}$ can be separated by a plane if and only if the characteristic equation has two distinct positive roots. It is not required to exactly determine the roots, but the existance - e.g. using Sturm-sequences (Hook and McAree 1990) - of two positive roots is sufficient to conclude that the ellipsoides are separated.

An important aspect is the enlargement of all radii of an ellipsoid by $\Delta r = \varepsilon r_2$, where being a userdefined constant. This approach is physically motivated by (Wittmann *et al.* 1985), who showed that aggregates are surrounded by a thin film of mortar. From the numerical point of view, this procedure is essential to define a minimum distance between ellipsoides and, consequently, non-distorted elements in the meshing procedure.

The randomness in the spatial location and the orientation of the particles reflects the stochastic character of the arrangement of particles in a real model. Different realizations of the particle arrangement can be obtained by modifying the seed of the random number generator used for the generation of the random locations and orientations, thus the variability of the response with respect to varying particle arrangement can be investigated.

In order to generate a 2-dimensional model, a slice of the 3-dimensional model is used, where ellipses with a radius smaller than a prescribed treshold related to the mesh size are removed.

3. Material formulations for the constituents

For normal strength concrete, it is seldom observed that cracks pass through the aggregates. As a consequence, the aggregates are assumed to be linear elastic. Due to the small dimension of the ITZ, it is modeled with a discrete crack concept applying a cohesive formulation, whereas the matrix material is simulated using a combined damage/plasticity formulation.

3.1 Plasticity model combined with nonlocal isotropic damage for the matrix

Pure plastic models are not capable of simulating the stiffness degradation, which is observed in experiments. By contrast, pure damage models are not able to represent irreversible deformations. A combination of both approaches can overcome these deficiencies. The combination of plasticity with damage is usually based on an isotropic plasticity model combined either with an anisotropic damage model as e.g. in (Carol *et al.* 2001, Hansen *et al.* 2001), or an isotropic damage model.

The plasticity model can either be formulated in the effective stress space (i.e. the undamaged stress space) as e.g. in (Ju 1989, Jason *et al.* 2006). Another choice is a formulation in the nominal stress space (i.e. the damage stress space) as in (Lubliner *et al.* 1989, Ananiev and Ožbolt 2004). Grassl investigated the two different approaches with respect to the local uniqueness conditions (Grassl and Jirásek 2004), which means, whether for a prescribed strain history a unique response in terms of stresses and history variables is obtained. The formulation in the effective stress space fulfilled these conditions without any further restrictions, whereas for the formulation in the nominal stress space certain restrictions for the plasticity model (e.g. a plasticity model with hardening) have been found.

In the current work, a plasticity formulation for small strains in the effective stress space combined with an isotropic damage model similar to (Grassl and Jirásek 2006) has been used.

An advantage from a numerical point of view is that the formulation in the effective stress space further allows a decoupling of the return mapping algorithm for the plasticity solution from the damage evolution.

The stress-strain relation is given by

$$\boldsymbol{\sigma} = (1-\omega)\boldsymbol{C}:(\varepsilon-\varepsilon^p) \tag{20}$$

$$= (1-\omega)\bar{\boldsymbol{\sigma}} \tag{21}$$

where $\boldsymbol{\sigma}$ is the stress tensor, $\boldsymbol{C}$ the elastic material matrix, ε the total strain, ε^p the plastic strain, $\bar{\boldsymbol{\sigma}}$ the effective stress. For $\omega = 0$, the model corresponds to a plasticity model, whereas for $\varepsilon^p = 0$ a pure damage model is obtained.

First, the plasticity model is presented, afterwards the local damage formulation is added, and, finally, the extension to the nonlocal damage model is made.

3.1.1 Plasticity formulation

An associated plasticity model defined in the effective stress space $\bar{\boldsymbol{\sigma}}$ is used. For multisurface plasticity, the evolution of the plastic strain is governed by Koiters rule

$$\dot{\varepsilon}^p = \sum_{i=1}^{m} \dot{\gamma}_i \frac{\partial f_i^p}{\partial \bar{\boldsymbol{\sigma}}} \tag{22}$$

where f_i^p are the yield functions of the plasticity model and γ_i the corresponding plastic multipliers. The Karush-Kuhn-Tucker conditions are given by

$$f_i^p \le 0 \qquad \dot{\gamma}_i \ge 0 \qquad f_i^p \dot{\gamma}_i = 0 \qquad \forall i \tag{23}$$

In this work, hardening is not considered in the model. Three different yield surfaces have been investigated Rankine, Drucker-Prager and a combination of both within a multisurface plasticity approach. For the Rankine model, the rounded yield surface is defined by

$$f_{RK}^{p} = \begin{Bmatrix} \sigma_{\mathrm{I}} - f_{ct} & \sigma_{\mathrm{II,III}} < 0 \\ \sqrt{\sigma_{\mathrm{I}}^2 + \sigma_{\mathrm{II}}^2} - f_{ct} & \sigma_{\mathrm{III}} < 0 \\ \sqrt{\sigma_{\mathrm{I}}^2 + \sigma_{\mathrm{II}}^2 + \sigma_{\mathrm{III}}^2} - f_{ct} & \sigma_{\mathrm{I,II,III}} \geq 0 \end{Bmatrix} \tag{24}$$

with the principal stresses $\sigma_{\mathrm{III}} \leq \sigma_{\mathrm{II}} \leq \sigma_{\mathrm{I}}$ and the uniaxial tensile strength f_{ct}.

The Drucker-Prager yield surface is defined by

$$f_{DP}^{p} = \frac{\beta}{3} I_1 + \sqrt{J_2} - H_p \tag{25}$$

where I_1 is the first invariant of the stress tensor and J_2 the second invariant of its deviator. The material parameters β and H_p can be determined from the unixial compressive strength f_c and the biaxial compressive strength f_{c2}

$$\beta = \frac{\sqrt{3}(f_{c2} - f_c)}{2f_{c2} - f_c} \tag{26}$$

$$H_p = \frac{f_{c2} f_c}{\sqrt{3}(2f_{c2} - f_c)} \tag{27}$$

Further details about the numerical implementation can be found in Appendix A.

The Drucker-Prager yield surface gives a good approximation of the material behavior of concrete in compression. Other material laws for concrete in compression additionally include the Lode angle (or equivalently, the third invariant of the stress tensor), which has not been considered in this work. One of the main purposes of mesoscale simulations is the assumption that simple material formulations for each component lead to a complex response due to the geometrical distribution and the interaction of the components.

The Rankine criterion is a good approximation in tension. Consequently, a combination of both yield criteria to model tension as well as compression has been implemented, as illustrated in Fig. 2.

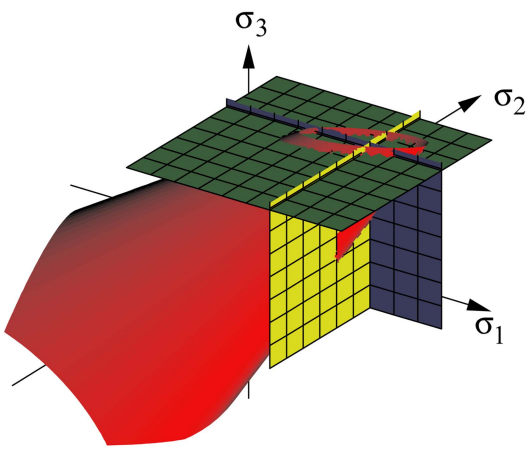

Fig. 2 Rankine and Drucker-Prager yield surfaces and the principal stress space

By using the rounded Rankine criterion no auxiliary yield function is required. Due to the decoupling of plasticity and damage, a return mapping algorithm for the plastic part of the model with multisurface plasticity according to (Simo and Hughes 1997) can be used.

Application of an implicit backward Euler difference scheme to Eqs. (22), (23) and (21) gives the following coupled system of equations

$$\bar{\boldsymbol{\sigma}}_{n+1} = \boldsymbol{C}(\varepsilon_{n+1} - \varepsilon^p_{n+1}) \tag{28}$$

$$\varepsilon^p_{n+1} = \varepsilon^p_n + \sum_{\alpha=1}^{m} \Delta\gamma_\alpha \frac{\partial f^p_\alpha(\bar{\boldsymbol{\sigma}}_n + 1)}{\partial \bar{\boldsymbol{\sigma}}} \tag{29}$$

$$f^p_\alpha(\bar{\boldsymbol{\sigma}}_{n+1}) \le 0 \tag{30}$$

$$\Delta\gamma_\alpha \ge 0 \tag{31}$$

$$\Delta\gamma_\alpha f^p_\alpha(\bar{\boldsymbol{\sigma}}_{n+1}) = 0 \tag{32}$$

which is solved for the plastic multipliers $\Delta\gamma_\alpha$, the plastic strains ε^p and the effective stresses $\bar{\boldsymbol{\sigma}}$. During the iterative solution of the coupled system of equations using a Newton-iteration as explained in detail in (Simo and Hughes 1997), it is required to update the active yield functions. For each intermediate state in the Newton iteration, the Karush-Kuhn-Tucker conditions are verified. If the plastic multiplier for a formerly active yield function is negativ, the yield function is removed from the set of active functions. Similarly, if the value of a yield function that is not part of the active set is positive, the function is added to the active set. In general, this procedure converges. However for certain situations, an oscillating behavior was experienced, where a yield function was added in one step and removed in the next one. In such a situation, where convergence after a certain number of iterations is not achieved, all possible sets of active yield functions are checked. Within each of these iterations, the set of active functions remains constant. After convergence of the procedure (all active yield functions are equal to zero), consistency of the solution is verfied, i.e. if all other yield functions/plastic multiplier fulfill the Karush-Kuhn-Tucker conditions.

The nonlinear iteration on the system level is solved using a full Newton-Raphson iteration, which requires the determination of an algorithmic elastoplastic tangent modulus. Differentiation of Eqs. (28) and (29) and rearranging finally gives

$$\frac{d\bar{\boldsymbol{\sigma}}_{n+1}}{d\varepsilon_{n+1}} = \Sigma - \Sigma[\partial_\sigma \boldsymbol{f}^p(\bar{\boldsymbol{\sigma}}_{n+1})]^T \{\partial_\sigma \boldsymbol{f}^p(\bar{\boldsymbol{\sigma}}_{n+1})\Sigma[\partial_\sigma \boldsymbol{f}^p(\bar{\boldsymbol{\sigma}}_{n+1})]^T\}^{-1} \partial_\sigma \boldsymbol{f}^p(\bar{\boldsymbol{\sigma}}_{n+1})\Sigma \tag{33}$$

$$\Sigma = \left[C^{-1} + \sum_{\alpha: f_\alpha \in \mathcal{J}} \Delta\gamma_\alpha \frac{\partial^2 f^p_\alpha(\bar{\boldsymbol{\sigma}}_{n+1})}{\partial \boldsymbol{\sigma}^2} \right]^{-1} \tag{34}$$

where $\mathcal{J}$ is the set of active yield functions. It is further to be noted that Σ is symmetric, which simplifies the computational effort. In combination with the damage formulation, the algorithmic tangent of the plastic strains with respect to the total strains is required. This can be derived from differentiation of Eq. (28)

$$\frac{d\boldsymbol{\sigma}_{n+1}}{d\varepsilon_{n+1}} = \boldsymbol{C} - \boldsymbol{C}\frac{d\varepsilon^p_{n+1}}{d\varepsilon_{n+1}} \tag{35}$$

Rearranging Eq. (35) gives the required expression

$$\frac{d\varepsilon_{n+1}^{p}}{d\varepsilon_{n+1}} = \boldsymbol{C}^{-1}\left(C - \frac{d\bar{\boldsymbol{\sigma}}_{n+1}}{d\varepsilon_{n+1}}\right) \tag{36}$$

where $\frac{d\bar{\boldsymbol{\sigma}}_{n+1}}{d\varepsilon_{n+1}}$ can be calculated from Eq. (33).

3.1.2 Local damage formulation

The proposed material law should be used within a mesoscale approach to model the soft matrix, which is surrounded by hard aggregates. For this scale, it is sufficient to simulate damage with an isotropic damage model, since the anisotropy of the global response is implicitly comprised in the mesoscale model. Several choices for the description of damage are possible, i.e. as a function of the stresses, the total strains or the plastic strains. In the presented model, the definition of a damage model as a function of the equivalent plastic strains has been used. Plasticity and damage start at the same time, and the elastic region is fully described by the yield function of the plasticity model. This corresponds to the assumption that relocations in the microstructure at the elastic limit are described by the plasticity model, but simultaneously lead to damage within the microstructure. With this approach, hardening in the prepeak region of the load-displacement curve cannot be captured. However, this phenomena is included in the mesomodel due to the successive creation of microcracks, which coalesce only in the post-peak region into macroscopic cracks. The damage model is described by the evolution law, the loading function and the loading/unloading conditions. The loading function is given by

$$f^{d}(\varepsilon^{p}) = \left\|\varepsilon^{p}\right\| - \kappa \tag{37}$$

with the loading/unloading conditions

$$f^{d} \le 0 \qquad \dot{\kappa} \ge 0 \qquad f^{d}\dot{\kappa} = 0 \tag{38}$$

where $\left\|\varepsilon^{p}\right\|$ is the equivalent plastic strain. The damage evolution is given by

$$\omega = 1 - e^{-\frac{\kappa}{\varepsilon_f}} \tag{39}$$

The parameter ε_f is a parameter that is related to the fracture energy G of the material and the equivalente length l_{eq}, which is a parameter of the finite element model and describes the influence radius of the corresponding material point, i.e. the dimension of the element that includes this material point. This parameter can be determined from the area under the stress-strain curve.

3.1.3 Nonlocal damage formulation

The mesh sensitivity of the local formulation is reduced by introducing the factor l_{eq} that accounts for the thickness of the local zones of damage. However, the zone of damage decreases with the meshsize and, in general, damage localizes only in one row of elements. Furthermore, the calculation of the equivalent lenght is not straightforward, since for different orientations of the element with respect to the loading direction a modification of the equivalente lenght would be required. In order to circumvent these drawbacks, a nonlocal formulation is used. In nonlocal formulations, certain variables are replaced by their nonlocal average. If t is a local field, its nonlocal counterpart is given by

$$\bar{t}(\boldsymbol{x}) = \int_{V} w(\boldsymbol{x}, \boldsymbol{\xi}) t(\boldsymbol{\xi}) d\xi \tag{40}$$

where $w(\mathbf{x}, \boldsymbol{\xi})$ is a given weight function. For an isotropic weight function, the weight depends only

on the distance r between source and target point. Furthermore, the weight function is scaled, so that a uniform field t is identical to its nonlocal counterpart $\bar{t}$. In this work, the rescaled bell-shaped weighting function is used

$$w(\boldsymbol{x},\boldsymbol{\xi}) = \frac{\alpha(\|\boldsymbol{x}-\boldsymbol{\xi}\|)}{\int_V \alpha(\|\boldsymbol{x}-\boldsymbol{\eta}\|)\,d\boldsymbol{\eta}} \tag{41}$$

$$\alpha(r) = \begin{Bmatrix} \left(1-\dfrac{r^2}{R^2}\right)^2 & r<R \\ 0 & r\geq R \end{Bmatrix} \tag{42}$$

(Jirásek 1998) investigated nonlocal models with respect to their capability to describe the material until final failure. For certain nonlocal formulations, locking phenomena occured and the material response could only be correctly approximated close to the peak of the load-displacement curve. For nonlocal models of the form

$$\boldsymbol{\sigma} = (1-\omega(\bar{\varepsilon}))\boldsymbol{C}\varepsilon \tag{43}$$

no locking phenomena were found. In this context, a second variant was investigated where not the strain is averaged, but the equivalent strain. Both variants have been investigated, but no substantial difference in the results has been realized. Due to numerical reasons, the second variant has been finally applied, since for the nonlocal averaging only a scalar variable has to be computed, whereas in Eq. (43) a field of up to six variables (depending on the number of plastic strain components) has to be averaged. In the nonlocal formulation, the evolution law is replaced by

$$\omega = 1-e^{-\frac{\bar{\kappa}}{\varepsilon_f}} \tag{44}$$

where κ is the local equivalent plastic strain and $\bar{\kappa}$ its nonlocal counterpart calculated using Eq. (40). For a uniaxial tensile test it is observed that with the presented nonlocal formulation, constant plastic strains localize in a single element, whereas in the neighboring elements almost no plastic strains are observed. By contrast (due to the nonlocal formulation), damage is generated in the whole region of the nonlocal influence radius. It is furthermore noted that most of the inelastic energy is dissipated in the single element with the localization, which is explained by the large plastic strains within this element.

The determination of the nonlocal radius is a severe problem. Many researchers claim that this nonlocal radius R is a material property. This seems to be reasonable, since the size of the fracture process zone is related to the intrinsic material length of the material. (Grassl and Jirásek 2010) investigated the size of the fracture process zone from mesoscale simulations using lattice models in order to determine an appropriate nonlocal radius for different weighting functions. For concrete, it was found that the size of the fracture process zone relates to the size of the largest particles in the model. Fixing the nonlocal radius as a material property, the parameter ε_f is directly related to the specific fracture energy of the material. As a consequence, two of the three parameters ε_f, R and G can be defined by the user, whereas the third parameter can directly be calculated

$$\varepsilon_f = \frac{15G}{16 f_{ct} R} \tag{45}$$

Eq. (45) is obtained by integration of the stress-strain curve with localized plastic strains in a single element.

The algorithmic stiffness for the combined model can be derived by differentiation of Eq. (20)

$$\frac{d\boldsymbol{\sigma}^{(i)}}{d\varepsilon^{(j)}} = \frac{\partial\omega^{(i)}}{\partial\bar{\kappa}^{(i)}}\frac{\partial\bar{\kappa}^{(i)}}{\partial\bar{\kappa}^{(j)}}\frac{\partial\bar{\kappa}^{(j)}}{\partial\varepsilon_p^{(j)}}\frac{\partial\varepsilon_p^{(j)}}{\partial\varepsilon^{(j)}}\bar{\boldsymbol{\sigma}}^{(i)} + \delta_{ij}(1-\omega)\left(\boldsymbol{C} - \boldsymbol{C}\frac{\partial\varepsilon^{p(i)}}{\partial\varepsilon^{p(j)}}\right) \tag{46}$$

which can be evaluated using Eqs. (44), (40) and Eq. (36). The indices i and j reference the intergration points. In this context it is to be noted that the stiffness matrix is no longer symmetric. This is due to the rescaling of the weighting function, which results in unsymmetric weights and is related to boundary effects (Krayani *et al.* 2009). In the current mesoscale model, it is especially important to reduce the influence of these boundary effects, since there are many internal boundaries due to the different material formulation for matrix and particles. However, in this model, the cohesive interface has a smaller tensile strength compared to the matrix. As a result, the smeared crack in the nonlocal model is almost perpendicular to the boundaries between matrix and particles, which reduces the boundary effect dramatically. In contrast, investigations using models without cohesive interface elements, in which the interface crack around a particle had to be simulated as a crack solely within the matrix showed strong boundary effects.

It is further to be noted that the stresses within an element depend on all strains within the nonlocal radius. Consequently, the element stiffness matrix is not quadratic, but has a rectangular shape.

3.2 Cohesive interface formulation for the ITZ

In order to describe cracking phenomena in quasibrittle materials, Hillerborg developed the fictitious crack model (Hillerborg *et al.* 1976). The model is an extension of the Dugdale/Barenblatt plastic crack-tip model (Dugdale 1960, Barenblatt 1962), which relates normal stress and normal crack opening. It is based on the idea that, close to the crack tip, stresses between opposite faces of the crack can be transfered by mechanisms such as aggregate interlocking, friction and material bonding.

In the current work, a model based on (Tvergaard 2003; Ortiz and Pandolfi 1999) is used, which describes normal as well as tangential tractions along an interface. A total crack opening λ is introduced

$$\lambda = \sqrt{\langle u_n^2 \rangle + (\alpha u_t)^2} \tag{47}$$

where u_n and u_t are the normal opening and tangential sliding of the interface surfaces, and α is a material constant which controls the weighting between the normal and tangential opening. Note that by using the McCauly brackets, only a positive normal crack opening contributes to the total crack opening. Furthermore, a cohesive traction-separation law is used for loading conditions

$$\sigma(\lambda) = \begin{cases} K_p\lambda & \lambda < \lambda_0 \\ f_{ct}e^{\frac{-f_{ct}(\lambda-\lambda_0)}{G_f}} & \text{otherwise} \end{cases} \tag{48}$$

where $\lambda_0 = f_{ct}/K_p$ is the crack opening at which the linear elastic peak load is reached, K_p is the penalty stiffness, f_{ct} the tensile strength of the interface layer and G_f its fracture energy. The penalty part is important to allow a crack to remain closed for compressive stresses and small tensile stresses.

Assuming that a potential Φ

$$\Phi(u_n, u_t) = \int_0^{\lambda(u_n, u_t)} \sigma(\lambda')d\lambda' \tag{49}$$

exists, the normal and tangential tractions are obtained respectively by

$$T_n = \frac{\partial \Phi(u_n, u_t)}{\partial u_n} = \sigma(\lambda)\frac{u_n}{\lambda} \tag{50}$$

$$T_t = \frac{\partial \Phi(u_n, u_t)}{\partial u_t} = \sigma(\lambda)\frac{\alpha^2 u_t}{\lambda} \tag{51}$$

Describing the total potential as a function of the mixed displacement λ leads to the assumption that the fracture energies for mode I and mode II are equivalent, although this differs from the general assumption that the mode II fracture energy for concrete is higher than the mode I fracture energy. However, an advantage for the numerical implementation is that the obtained stiffness matrix is symmetric. The penalty stiffness K_p must be chosen carefully. On the one hand, the penetration of the two adjacent crack faces of the interface in compression has to be reduced by making K_p as large as possible. On the other hand, a high penalty stiffness results in an ill-conditioned global stiffness matrix. In the implementation of the model, the penalty stiffness was determined using an empirical approach.

A history variable λ_{max}, which corresponds to the maximum total crack opening λ reached during loading, is required to decide, whether the material point is under loading ($\lambda \geq \lambda_{max}$) or unloading ($\lambda < \lambda_{max}$) conditions. A damage model is applied for the unloading path, and a linear function back to the origin is assumed

$$T_n = \sigma(\lambda_{max})\frac{u_n}{\lambda_{max}} \tag{52}$$

$$T_t = \sigma(\lambda_{max})\frac{\alpha^2 u_t}{\lambda_{max}} \tag{53}$$

If the interface is in compression, the contact condition is approximated by the penalty stiffness

$$T_n = K_p u_n \tag{54}$$

and the parameter λ is only a function of the tangential displacement

$$\lambda = |\alpha u_t| \tag{55}$$

4. Numerical results

4.1 Tensile test

In a first example, a tensile test performed by (Kessler-Kramer 2002) was used. The geometry is illustrated in Fig. 3. The main advantage of this test compared to many others is the fact that there is no prescribed notch, which triggers the localization. As a consequence, the particle distribution has a much more pronounced but nontheless more realistic effect compared to a notched specimen. In order to simplify the numerical model, only the inner part with a width of 60 cm is modeled,

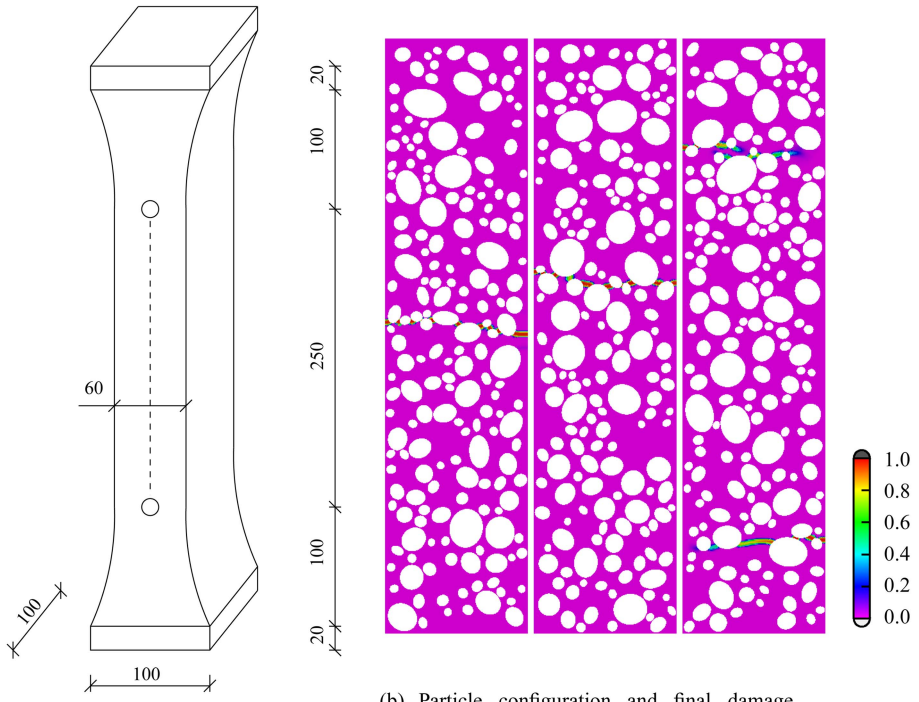

(a) Geometry

(b) Particle configuration and final damage distribution of three samples

Fig. 3 Geometry and final damage distribution of the tensile test performed by (Kessler-Kramer 2002) for varying particle distributions

Table 1 Material parameters for the numerical simulation of the tensile test (Kessler-Kramer 2002)

Parameter			Matrix	Interface	Aggregate
Young's modulus	E	$\left[\frac{N}{mm^2}\right]$	≈27500†	-	55000
Poisson's ratio	ν	$[-]$	0.18	-	0.2
Tensile strength	f_{ct}	$\left[\frac{N}{mm^2}\right]$	3.9	2.93	-
Uniaxial compressive strength	f_c	$\left[\frac{N}{mm^2}\right]$	39	-	-
Biaxial compressive strength	f_{c2}	$\left[\frac{N}{mm^2}\right]$	45.2	-	-
Fracture energy	G	$\left[\frac{Nmm}{mm^2}\right]$	0.219	0.164	-
Nonlocal radius	r	$[mm]$	1.5	-	-
Interaction value	a	$[-]$	-	1	-

† The parameter was calculated from the macroscopic Young's modulus 33930 $\frac{N}{mm^2}$ and the actual fraction of aggregates using Eq. (56).

which correponds to the region over which the relative displacements are measured in the experiment. Strong boundary effects, e.g. that damage develops especially in the boundary layer triggered by the stiffer displacement constraints (compared to the experiment) was not observed. The material parameters used in the simulation are summarized in Table 1. The grading curve was taken from (Kessler-Kramer 2002), where the total amount of aggregates is given by 77 mass-%, partitioned into 24.6 mass-% in the class 8/16, 29.2 mass-% in the class 2/8 and 23.1 mass-% homogenized in the matrix material with a diameter smaller than 2 mm. The Young's modulus of the matrix Em was determined using the Reuss formula (Reuss 1929). By assuming the Young's modulus of the particles to be twice the Young's modulus of the matrix, the following relation is obtained

$$\frac{1}{E_c} = \frac{\rho_m}{E_m} + \frac{1-\rho_m}{2E_m} \tag{56}$$

where ρ_m is the volume fraction of the matrix and E_c the macroscopic Young's modulus of concrete. An alternative possibility is to fix the Young's modulus of the particles and compute the Young's modulus of the matrix.

On the basis of 50 simulations, the influence of the particle distribution on the load-displacement curve is evaluated. In Fig. 3(b) the particle distribution and the damage at the final load-step for the first three samples is illustrated. It is observed that the particle configuration has a substantial influence on the location of the final crack. Furthermore, cracks are passing primarily along grain boundaries, and matrix cracks are only obtained when these cracks in the interface layer coalesce. In the initial stage, many microcracks depicted by zones of local damage are obtained. In general, the final failure mode is a single crack which has been developed from these microcracks. It sometimes happens - as in the right sample in Fig. 3(b) - that two competing cracks are obtained and the localization into a single crack is obtained only at an advanced loading level.

The mean and the standard deviation of the corresponding load-displacement curves are illustrated in Fig. 4. It is observed that the particle distribution primarily influences the post-peak branch - the peak load is only slightly influenced. This is due to the fact that the particles primarily influence the crack path and, consequently, the length over which energy is dissipated.

4.2 Compression test 3D

In a second example, a compression test of a concrete cube is performed in 3D and compared to

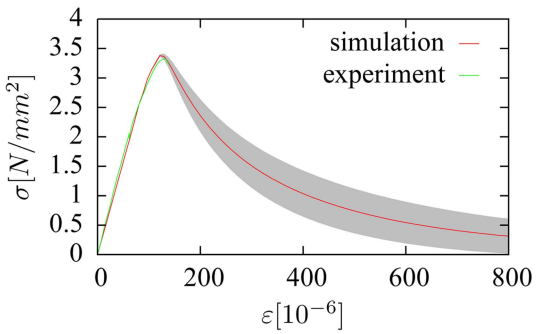

Fig. 4 Influence of particle distribution on the load-displacement curve

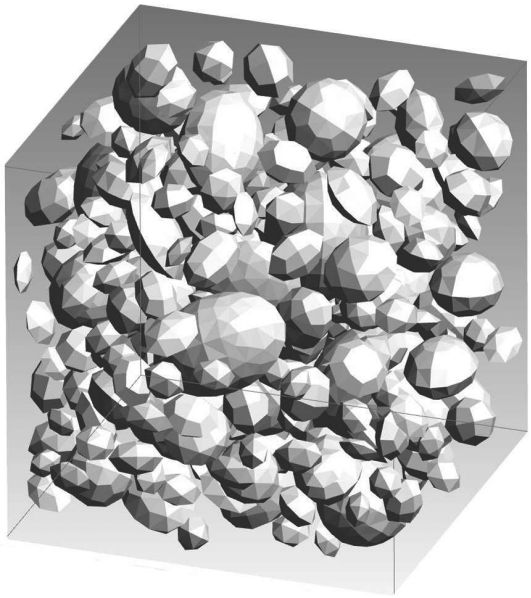

Fig. 5 Particles simulated in the concrete cube with edge length 25 mm

Table 2 Material parameters for the 3-dimensional compression test

Parameter			Matrix	Interface	Aggregate
Young's modulus	E	$\left[\frac{N}{mm^2}\right]$	26738	-	53476.1
Poisson's ratio	ν	[−]	0.18	-	0.18
Tensile strength	f_{ct}	$\left[\frac{N}{mm^2}\right]$	3.4	f_i·3.4	-
Uniaxial compressive strength	f_c	$\left[\frac{N}{mm^2}\right]$	50	-	-
Biaxial compressive strength	f_{c2}	$\left[\frac{N}{mm^2}\right]$	58	-	-
Fracture energy	G	$\left[\frac{Nmm}{mm^2}\right]$	0.12	G_i·0.12	-
Nonlocal radius	r	$[mm]$	1	-	-
Interaction value	α	[−]	-	1	-

experimental data from (van Vliet and van Mier 1995). In contrast to a tensile test, where the failure state can be calculated in 2D, the compression test has to be performed in 3D in order to accurately capture the failure mechanism.

The experimentally tested concrete cube has a side length of 100 mm. In the numerical simulation, a concrete cube with a side length of 25 mm has been used and the results were scaled

for comparison.

The full cube could not be simulated numerically due to the large number of dofs and the mesh creation in 3D. The upper and lower boundary conditions correspond to high friction between the cube and the loading platens. According to a prescribed grading curve, 39 ellipsoids in in the class 4-8 mm where placed into the specimen, and 230 ellipsoids in the class 2-4 mm, which is illustrated in Fig. 5. The matrix is assumed to include all the particles smaller than 2 mm. The material parameters used in the simulation are summarized in Table 2. It is important to mention that no parameter fitting has been performed. The fracture energy of the matrix was set to the experimental fracture energy of the macroscopic concrete specimen, which is only an approximation. Due to the increased fracture surface in a mesoscale tensile test, the fracture energy of the matrix is slightly smaller compared to the macroscopic model. Due to lack of additional information, the fracture energy and the tensile strength of the interface where chosen to be a multiple of the corresponding parameters of the matrix. The factor was chosen to be 90%, which assures that the cracks around the particles propagate along the interface elements. If cracks around the particle develop in the matrix with the crack being almost parallel to the interface between matrix and particle, boundary effects due to the renormalization of the nonlocal weighting function occur, and the assumption of energy dissipation in the full range of the nonlocal radius is not valid any more.

Additionally, the influence of different yield functions used in the plasticity model has been investigated (Rankine, Drucker-Prager and combination of both) and compared to the isotropic damage model. In Fig. 6, the damage distribution at the end of the calculation is illustrated. One of the main motivations for using mesoscale models was the idea to represent the complex macroscopic response by dissolving the heterogenuous mesostructure in the numerical model and applying simple material formulations to each of the constituents. For that matter it was assumed that the compressive failure of concrete could be modeled by using a mesoscale model with matrix failure defined by a criterion in tension as e.g. the Rankine yield surface. The damage pattern in Fig. 6(b) does no coincide with the experimental results obtained for a compression test of concrete with high friction between the platens and the cube. Furthermore, no global softening behavior could be observed as illustrated in Fig. 7. At the ultimate applied displacement, columns of intact material transmitted high compressive forces. They were separated by vertical cracks, which

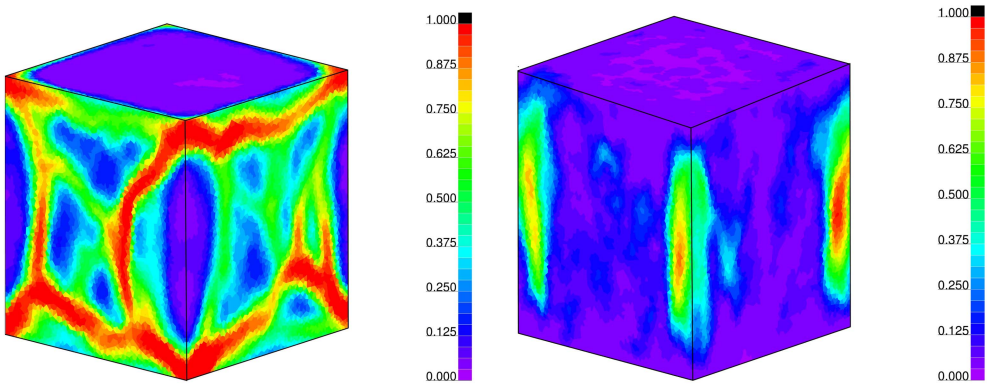

(a) Drucker-Prager and Rankine (b) Rankine yield function

Fig. 6 Damage distribution after the final load step of a uniaxial compression test for different yield functions of the matrix material using the combined damage-plasticity model

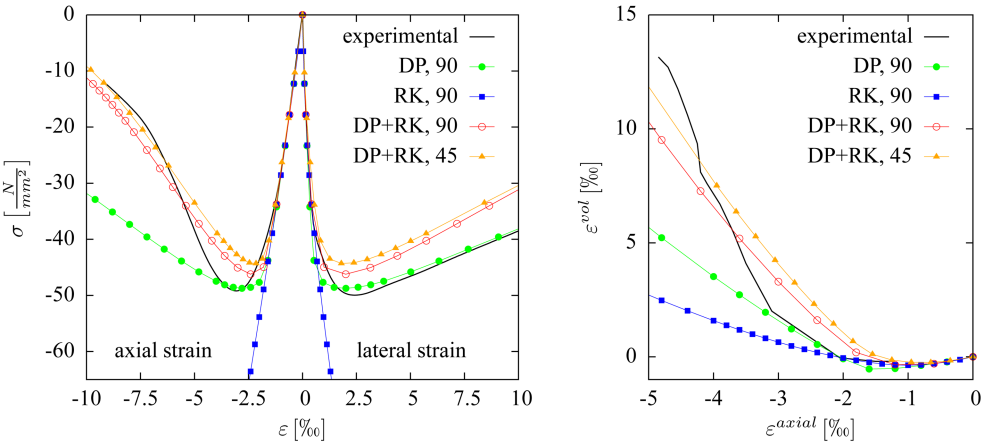

(a) Axial/lateral strain versus stress (b) Axial versus volumetric strain

Fig. 7 Uniaxial compression test in 3D of a cube with edge length 25 mm for different yield surfaces and G_i and f_i varied between 45% and 90% (DP: combined Drucker-Prager, RK: combined Rankine)

developed due to the lateral strain in the matrix. An alternative formulation was based on a pure Drucker-Prager criterion, where the cone of the failure surface was determined from the uniaxial and biaxial compressive strengths. In most numerical simulations, the latter was estimated from the unixial compressive strength. The Drucker-Prager yield surface is often used to describe failure of concrete in compression. The failure pattern corresponds to the experimental results similar to the combined approach, where curved shear zones develop, which finally lead to spalling of the vertical edges. Additionally, softening of the global response can be simulated. The onset of failure is accurately captured by the model, as well as the lateral strain (which is calculated from the lateral displacements at the midsection). The fracture energy in compression is overestimated by the numerical model, which is probably due to the fact that the parameter ε_f is calibrated from a tensile test. Furthermore, a combination of the Rankine criterion for tension and the Drucker-Prager criterion in compression in the framework of a multiplasticity approach was investigated. The onset of material degradation was slightly earlier compared to the Drucker-Prager model. The simulated axial stress-strain diagramm is close to the experimental data, although the compressive strength is slightly smaller in the numerical model, which is probably due to the parameter set (no fitting). In a similar way, the difference in the lateral strain can be explained. The volumetric expansion (dilatation) is best approximated with the combined model. The interface parameters, i.e. the factor relating the fracture energy and the tensile strength of the interface to the corresponding parameters of the matrix, have only a minor influence. This might be attributed to the small number of particles considered in the simulation. A second reason is probably the fact that in a compression test the primary failure domain is the matrix. Interface cracks seem to have only a minor influence.

5. Conclusions

In the present paper, a mesoscale model for concrete has been presented. This allows a more realistic simulation of the nonlinear behavior. Microcracks, which primarily initiate along particle

boundaries finally coalesce into a macroscopic crack. Particles are assumed to be represented by ellipsoids, whose size distribution is generated according to prescribed grading curves. Zones of local failure within the model are either represented by interface cracks in the ITZ simulated with a cohesive model, or by a constitutive model for the matrix based on a plasticity formulation in the effective stress space using Drucker-Prager and Rankine yield surfaces combined with a nonlocal isotropic damage formulation as a function of the equivalent plastic strain. On the one hand, this model allows to implement one source of the stochastic scatter of experiments into the numerical model. On the other hand, the damage distribution on the mesoscale including microcracks is computed. This model might serve as a basis for coupled problems, where the damage distribution influences the constitutive parameters, e.g. the moisture transport, the thermal conductivity or chemical processes. Localization in uniaxial tests is automatically obtained without the requirement to predefine weakened sections. Furthermore, the complex nonlinear behavior on the macroscale can be simulated by simple formulations on the mesoscale, e.g. the nonlinear prepeak behavior can be represented without any hardening variables in the constitutive relations.

References

Ananiev, S. and Ožbolt, J. (2004), "Plastic damage model for concrete in principal directions", in V. Li, C. Leung, K. Willam, & S. Billington (Eds.), *Fracture Mech. Concrete Struct.*, 271-278.

Barenblatt, G. (1962), "The mathematical theory of equilibrium of cracks in brittle fracture", *Adv. Appl. Mech.*, **7**, 55-129.

Bazant, Z.P., Tabbara, M.R., Kazemi, M.T. and Pijaudier-Cabot, G. (1990), "Random particle model for fracture of aggregate or fiber composites", *J. Eng. Mech.*, **116**(8), 1686-1705.

Carol, I., Lopez, M. and Roa, O. (2002), "Micromechanical analysis of quasi-brittle materials using fracture-based interface elements", *Int. J. Numer. Meth. Eng.*, **52**(1-2), 193-215.

Carol, I., Rizzi, E. and Willam, K. (2001), "On the formulation of anisotropic elastic degradation : II. Generalized pseudo-rankine model for tensile damage", *Int. J. Solids Struct.*, **38**(4), 519-546.

Carpinteri, A. and Chiaia, B. (1995), "Multifractal nature of concrete fracture surfaces and size effects on nominal fracture energy", *Matériaux et Constructions*, **28**(182), 435-443.

Chiaia, B., Vervuurt, A. and Van Mier, J. (1997), "Lattice model evaluation of progressive failure in disordered particle composites", *Eng. Fract. Mech.*, **57**(2-3), 301-318.

d'Addetta, G. A. (2002), *Discrete models for cohesive fricional materials*, Ph.D. thesis, University of Stuttgart, Institute for Structural Mechanics.

Dugdale, D. (1960), "Yielding of sheets containing slits", *J. Mech. Phy. Solids*, **8**, 100-104.

Eckardt, S. and Könke, C. (2006), "Simulation of damage in concrete structures using multiscale methods", in N. Bianic, R. de Borst, H. Mang, & G. Meschke (Eds.), *Proceedings Intern. Conf. on Computational Modelling of Concrete Structures (EURO-C 2006).*

Eckardt, S. and Könke, C. (2008), "Adaptive damage simulation of concrete using heterogeneous multiscale models", *J. Algorithms Comput. Tech.*, **2**(2), 275-297.

Feldkamp, L.A., Goldstein, S.A., Parfitt, A.M., Jesion, G. and Kleerekoper, M. (1989), "The direct examination of three-dimensional bone architecture in vitro by computed tomography", *J. Bone Miner. Res.*, **4**(1), 3-11.

Garboci, E. (2002), "Three-dimensional mathematical analysis of particle shape using X-ray tomography and spherical harmonics: application to aggregates used in concrete", *Cement Concrete Res.*, **32**, 1621-1638.

Grassl, P. and Bažant, Z.P. (2009), "Random lattice-particle simulation of statistical size effect in quasi-brittle structures failing at crack initiation", *J. Eng. Mech.*, **135**(2), 85-92.

URL http://link.aip.org/link/?QEM/135/85/1.

Grassl, P. and Jirásek, M. (2004), "Damage-plastic model for concrete failure", *Int. J. Solids Struct.*, **43**(22-23), 7166-7196.

Grassl, P. and Jirásek, M. (2006), "Plastic model with non-local damage applied to concrete", *Int. J. Numer. Anal. Meth. Geomech.*, **30**(1), 71-90.
Grassl, P. and Jirásek, M. (2010), "Meso-scale approach to modelling the fracture process zone of concrete subjected to uniaxial tension", *Int. J. Solids Struct.*, **47**(7-8), 957-968.
Häfner, S., Eckardt, S. and Könke, C. (2003), "A geometrical inclusion-matrix model for the finite element analysis of concrete at multiple scales", *Proceedings of the 16th International Conference on the Application of Computer Science and Mathematics in Architecture and Civil Engineering*, Weimar.
Häfner, S., Eckardt, S., Luther, T. and Könke, C. (2006), "Mesoscale modeling of concrete: geometry and numerics", *Comput. Struct.*, **84**(7), 450-461.
Hansen, E., Willam, K. and Carol, I. (2001), "A two-surface anisotropic damage/plasticity model for plain concrete", in R. de Borst, J. Mazars, G. Pijaudier-Cabot, & J. van Mier (Eds.), *Fract. Mech. Concrete Struct.*, 549-556.
Hillerborg, A., Modéer, M. and Petersson, P. (1976), "Analysis of crack formation and crack growth in concrete by means of fracture mechanics and finite elements", *Cement Concrete Res.*, **6**, 773-782.
Hollister, S.J. and Kikuchi, N. (1994), "Homogenization theory and digital imaging: a basis for studying the mechanics and design principles of bone tissue", *Biotech. Bioeng.*, **43**(7), 586-596.
Hook, D. and McAree, P. (1990), *Graphics gems, chap. Using sturm sequences to bracket real roots of polynomial equations*, 416-422, San Diego, CA, USA, Academic Press Professional, Inc.
Jason, L., Huerta, A., Pijaudier-Cabot, G. and Ghavamian, S. (2006), "An elastic plastic damage formulation for concrete: application to elementary tests and comparison with an isotropic damage model", *Comput. Method. Appl. M.*, **195**(52), 7077-7092.
Jirásek, M. (1998), "Nonlocal models for damage and fracture: comparison of approaches", *Int. J. Sol. Struct.*, **35**(31-32), 4133-4145.
Ju, J. (1989), "On energy-based coupled elastoplastic damage theories: constitutive modeling and computational aspects", *Int. J. Solids Struct.*, **25**(7), 803-833.
Kessler-Kramer, C. (2002), *Zugtragverhalten von Beton unter Ermüdungsbeanspruchung*, Ph.D. thesis, Universität Karlsruhe (TH), Germany.
Krayani, A., Pijaudier-Cabot, G. and Dufour, F. (2009), "Boundary effect on weight function in nonlocal damage model", *Eng. Fract. Mech.*, **76**(14), 2217-2231.
Leite, J., Slowik, V. and Mihashi, H. (2004), "Computer simulation of fracture processes of concrete using mesolevel models of lattice structures", *Cement Concrete Res.*, **34**(6), 1025-1033.
Leite, J.P.B., Slowik, V. and Apel, J. (2007), "Computational model of mesoscopic structure of concrete for simulation of fracture processes", *Comput. Struct.*, **85**(17-18), 1293-1303.
Lubliner, J., Oliver, J., Oller, S. and Oñate, E. (1989), "A plastic damage model for concrete", *Int. J. Solids Struct.*, **25**(3), 299-326.
Nagai, G., Yamada, T. and Wada, A. (2000), "Three-dimensional nonlinear finite element analysis of the macroscopic compressive failure of concrete materials based on real digital image", *Comp. Civil Build. Eng.*, **1**, 449-456.
Nagano, Y., Ikeda, Y. and Kawamoto, H. (2004), "Application of 3D X-RAY CT to stress simulation analysis of porous materials with homogenization method", in C. Miyasaka, Y. Yokono, D. Bray, & Cho (Eds.), *ASME/ JSME Pressure Vessels and Piping Conference, San Diego*, **484**, 141-146.
Ortiz, M. and Pandolfi, A. (1999), "Finite-deformation irreversible cohesive elements for three-dimensional crack-propagation analysis", *Int. J. Numer. Meth. Eng.*, **44**(9), 1267-1282.
Reuss, A. (1929), "Berechnung der Fließgrenze von Mischkristallen auf Grund der Plastizitätsbedingung für Einkristalle", *Zeitschrift für Angewandte Mathematikund Mechanik*, **9**(1), 49-58.
Schlangen, E. (1993), *Experimental and numerical analysis of fracture processes in concrete*, Ph.D. thesis, Delft University of technology.
Schlangen, E. and van Mier, J.G.M. (1992), "Simple lattice model for numerical simulation of fracture of concrete materials and structures", *Mater. Struct.*, **25**(9), 534-542.
Simo, J. and Hughes, T. (1997), *Computational inelasticity*, Springer-Verlag.
Sukumar, N., Chopp, D., Moßes, N. and Belytschko, T. (2001), "Modelling holes and inclusions by level sets in the extended finite-element method", *Comput. Method. Appl. M.*, **190**, 6183-6200.
Takano, N., Kimura, K., Zako, M. and Kubo, F. (2003), "Multi-scale analysis and microscopic stress evaluation for ceramics considering the random microstructures", *JSME Int. J. Series A - Solid M.*, **46**(4), 527-535.

Tvergaard, V. (2003), "Cohesive zone representation of failure between elastic or rigid solids and ductile solids", *Eng. Fract. Mech.*, **70**, 1859-1868.
Unger, J.F. and Könke, C. (2006), "Simulation of concrete using the extended finite element method", in N. Bićanić , R. de Borst, H. Mang, & G. Meschke (Eds.), *Proceedings Int. Conf. on Computational Modelling of Concrete Structures (EURO-C 2006)*, 239-247, Balkema.
van Vliet, M.R.A. and van Mier, J.G.M. (1995), "Softening behavior of concrete under uniaxial compression", in F. Wittman (Ed.), *Fracture mechanics of concrete structures (FraMCoS-2, Zürich)*, 383-396.
Vervuurt, A. (1997), *Interface fracture in concrete*, Ph.D. thesis, Delft University of technology.
Wang, W., Jiaye, W. and Myung-Soo, K. (2001), "An algebraic condition for the separation of two ellipsoids", *Comput. Aided Geom. D.*, **18**(6), 531-539.
Wang, Z., Kwan, A. and Chan, H. (1999), "Mesoscopic study of concrete I: Generation of random aggregate structure and finite element mesh", *Comput. Struct.*, **70**(5), 533-544.
Wittmann, F.H., Roelfstra, P.E. and Sadouki, H. (1985), "Simulation and analysis of composite structures", *Mater. Sci. Eng.*, **68**(2), 239-248.
Wriggers, P. and Moftah, S.O. (2006), "Mesoscale models for concrete: homogenisation and damage behaviour", *Finite Elem. Anal. Des.*, **42**(7), 623-636.
Zaitsev, Y.B. and Wittmann, F.H. (1981), "Simulation of crack propagation and failure of concrete", *Mater. Struct.*, **14**(5), 357-365.

NB

Appendix A. Numerical implementation of the multisurface plasticity model

Appendix A.1 Rankine model

For the Rankine model, the yield surface is defined by

$$f_{RK}^{p}=\begin{Bmatrix}\sigma_I-f_{ct} & \sigma_{\mathrm{II,III}}<0\\ \sqrt{\sigma_I^2-\sigma_{II}^2}-f_{ct} & \sigma_{\mathrm{III}}<0\\ \sqrt{\sigma_I^2+\sigma_{\mathrm{II}}^2+\sigma_{\mathrm{III}}^2}-f_{ct} & \sigma_{\mathrm{I,II,III}}\geq 0\end{Bmatrix} \tag{A.1}$$

with the principal stresses $\sigma_{\mathrm{III}} \leq \sigma_{\mathrm{II}} \leq \sigma_{\mathrm{I}}$ and the uniaxial tensile strength f_{ct}. The rounding of the yieldsurface has a physical meaning which corresponds to the assumption, that the yield function is influenced by the interaction between positive principal stresses. On the other hand, it is also due to numerical reasons, since singularities occur in the standard Rankine approach for the derivative of the yield function at stress states with $\sigma_{\mathrm{I}} = \sigma_{\mathrm{II}}$. In the present approach, the rounding was performed with the full radius σ_{I}, but smaller radii can be used as illustrated in Fig. A1 to obtain in the limit with $\sigma_M \rightarrow f_{ct}$ the standard Rankine yield surface.

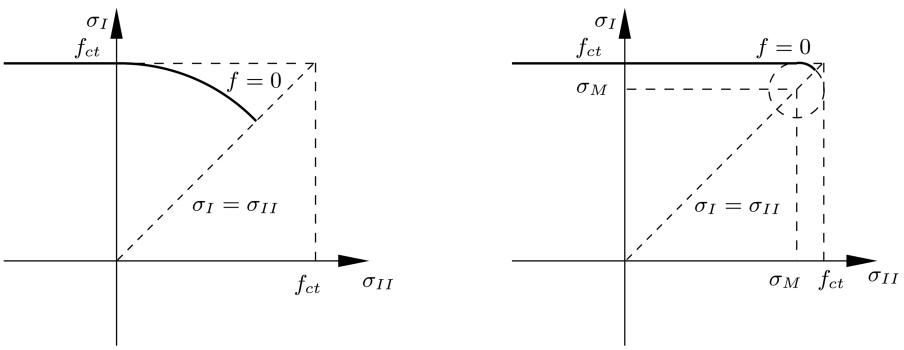

(a) Rounded rankine with radius $r = f_{ct}$ (b) Rounded rankine with radius $r < f_{ct}$

Fig. A1 Rounded Rankine criterion for plane stress

Appendix A.2 Drucker-Prager model

The Drucker-Prager yield surface corresponds to a cone in the principal stress space and has a singularity at the apex. In order to increase the stability and the convergence speed of the numerical solution close to this singularity, an auxilary yield function has been added

$$f_{aux}^{p}=\frac{\beta}{3}-\alpha H_p \tag{A.2}$$

with $\alpha = 0.9999$. This is illustrated in Fig. A2. Trial stress 1 is directly mapped to the Drucker-Prager yield surface. For trial stress 2, the auxiliary yield function is activated for the first iteration

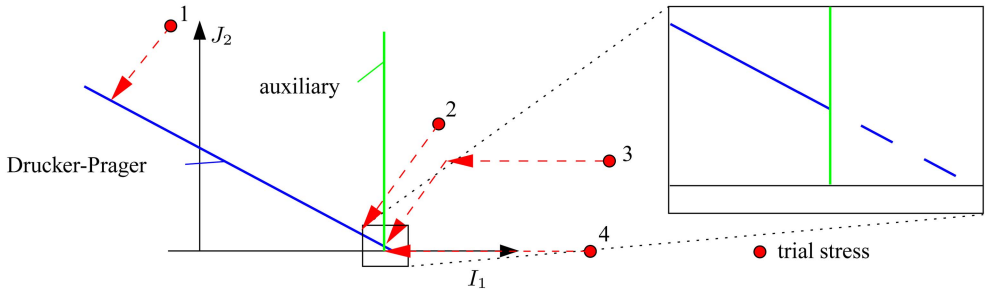

Fig. A2 Return mapping of trial stresses using the Drucker-Prager yield surface in combination with the auxiliary yield function

step of the return mapping, but finally deactived. Without the auxiliary function, numerical problems occur for trial stresses 3 and 4, but with the auxiliary yield function activated, they are both mapped back to the apex.